APL Materials

RESEARCH ARTICLE | JUNE 21 2022

Properties of high entropy borides synthesized via microwave-induced plasma

Special Collection: Design and Development of High Entropy Materials

Bria Storr ; Luke Moore; Kallol Chakrabarty ; Zaheeruddin Mohammed; Vijaya Rangari; Cheng-Chien Chen ; Shane A. Catledge

APL Mater. 10, 061109 (2022)
https://doi.org/10.1063/5.0098276
CHORUS

Properties of high entropy borides synthesized via microwave-induced plasma

Cite as: APL Mater. 10, 061109 (2022); doi: 10.1063/5.0098276
Submitted: 6 May 2022 • Accepted: 31 May 2022 •
Published Online: 21 June 2022

Bria Storr,[1] Luke Moore,[1] Kallol Chakrabarty,[1] Zaheeruddin Mohammed,[2] Vijaya Rangari,[2] Cheng-Chien Chen,[1,a)] and Shane A. Catledge[1,a)]

AFFILIATIONS

[1] Department of Physics, University of Alabama at Birmingham, Birmingham, Alabama 35294-1170, USA
[2] Department of Materials Science & Engineering, Tuskegee University, Tuskegee, Alabama 36088-1923, USA

Note: This paper is part of the Special Topic on Design and Development of High Entropy Materials.
[a)]**Present address:** Department of Physics, University of Alabama at Birmingham, 1300 University Blvd., 310 CH, Birmingham, Alabama 35294-1170, USA. **Authors to whom correspondence should be addressed:** chencc@uab.edu. **Tel.:** +1 (205) 934-8659 and catledge@uab.edu. **Tel.:** +1 (205) 934-3693.

ABSTRACT

Microwave-induced plasma was used to anneal precursor powders containing five metal oxides with carbon and boron carbide as reducing agents, resulting in high entropy boride ceramics. Measurements of hardness, phase structure, and oxidation resistance were investigated. Plasma annealing for 45 min in the range of 1500–2000 °C led to the formation of predominantly single-phase (Hf, Zr, Ti, Ta, Mo)B_2 or (Hf, Zr, Nb, Ta, Mo)B_2 hexagonal structures characteristic of high entropy borides. Oxidation resistance for these borides was improved by as much as a factor of ten when compared to conventional commercial diborides. Vickers and nanoindentation hardness measurements show the indentation size effect and were found to be as much as 50% higher than that reported for the same high entropy boride configuration made by other methods, with average values reaching up to 38 GPa (for the highest Vickers load of 200 gf). Density functional theory calculations with a partial occupation method showed that (Hf, Zr, Ti, Ta, Mo)B_2 has a higher hardness but a lower entropy forming ability compared to (Hf, Zr, Nb, Ta, Mo)B_2, which agrees with the experiments. Overall, these results indicate the strong potential of using microwave-induced plasma as a novel approach for synthesizing high entropy borides.

I. INTRODUCTION

High entropy ceramics are favorable candidates for applications in extreme environments due to their high melting point (>3000 °C), oxidation resistance, high hardness, resistance to thermal shock, and chemical inertness. Potential uses include hypersonic vehicles, nuclear energy management, wear-resistant coatings, thermoelectrics, and batteries.[1,2] High entropy borides (HEBs) are solid solutions typically containing five or more transition metal borides. They have a unique layered hexagonal crystal structure with alternating rigid two-dimensional (2D) boron nets and high entropy 2D layers of metal cations exhibiting mixed ionic and covalent metal-boron bonding. The configurational entropy of the solid-solution phase is maximized to stabilize it against the formation of intermetallics or other secondary phases to produce a maximum molar configurational entropy of $\Delta S_{mix} = R \ln N$, where N is the number of equimolar components and R is the gas constant.[3,4]

Recently, we have reported HEB synthesis via Boro–Carbo-Thermal-Reduction (BCTR) of a five-component transition metal oxide powder mixture (with B_4C and carbon black reducing agents) efficiently performed as a single annealing step by application of MicroWave (MW) plasma.[5] The plasma discharge can exert a significant effect in promoting rapid microwave heating processes and chemical reactions, as highly active species, such as electrons, ions, and radicals, can significantly enhance the reaction rate.[6] A low-temperature plasma is composed of neutral atoms and molecules, radicals, excited states, ions, and electrons with characteristic electron energies of a few eV and low degrees of ionization.[7] The energetic electrons can efficiently generate radicals, charged species, excited states, and photons. At the mean electron energies of a few eV that are common for the microwave plasma, vibrational

excitation is a dominant energy transfer pathway. Vibrational temperatures will be several thousands of degrees Celsius, while the translational (gas) temperatures may remain below 1000 °C. This creates a strongly non-equilibrium environment, which is considered to be favorable for chemical reactions.[8,9] Overall, the MW plasma approach is advantageous due to enhanced diffusion processes, reduced energy consumption, very rapid heating rates and considerably reduced processing times, decreased sintering temperatures via subsequent sintering steps, and improved physical and mechanical properties; features that are not typically associated with conventional processes.[10–13]

The objective of this work is to focus on two HEB systems: (Hf, Zr, Ti, Ta, Mo)B_2 and (Hf, Zr, Nb, Ta, Mo)B_2, particularly with regard to their structure, hardness, and oxidation resistance properties. These properties are evaluated along with computational modeling of the Entropy Forming Ability (EFA) and hardness as validation.[14,15] The EFA formalism has shown to be a powerful method in predicting the synthesizability of five-metal cubic carbides;[14] various high-EFA and high-hardness metal carbides were identified computationally by this approach and later confirmed experimentally. Our results demonstrate that the concept of EFA is also applicable to high entropy borides and that microwave-induced plasma can be utilized as a novel approach to synthesize high entropy borides with impressive mechanical properties for promising extreme-environment applications.

II. MATERIAL AND METHODS

The synthesis of near-equimolar high entropy transition metal borides, labeled here as HEB01 and HEB02 having nominal compositions of $(Hf_{0.2}Zr_{0.2}Ti_{0.2}Ta_{0.2}Mo_{0.2})B_2$ and $(Hf_{0.2}Zr_{0.2}Nb_{0.2}Ta_{0.2}Mo_{0.2})B_2$, respectively, was prepared to utilize BCTR facilitated by MW-induced plasma. The precursor powders included the metal oxides: hafnium oxide (HfO_2, 99%, 325 mesh; Alfa Aesar), zirconium oxide (ZrO_2, 99+%, 325 mesh; Alfa Aesar), tantalum pentoxide (Ta_2O_5, >60 mesh, 99%; Alfa Aesar), titanium oxide (TiO_2, 99.6%, 325 mesh; Alfa Aesar), niobium oxide (Nb_2O_5, 99+%, 325 mesh; Alfa Aesar), molybdenum oxide (MoO_3, <325 mesh, 99.95%; Alfa Aesar), carbon black (C, 99.99+%; Alfa Aesar), and boron carbide (B_4C, purity 99+%, 325 mesh; Alfa Aesar).

An adjustable microwave power of 1.3–1.5 kW and a chamber pressure of 2.4×10^4–3.3×10^4 Pa were used to anneal the pellet at 1500–2000 °C using microwave-induced plasma, as described in our previous work.[5] Briefly, the five metal oxides and carbon black were first blended using a high-energy ball mill (Spex 8000M, Spex SamplePrep Inc., NJ, USA) for 6 h with WC media and then combined with boron carbide. The precursor was dry milled for 2 h with WC balls and then wet milled for 4 h with zirconia balls in acetone. Due to the expected loss of boron during the annealing process, excess B_4C was added, as presented in Table I. The blended powder was dried at room temperature in a vacuum oven and then passed through a 200-mesh sieve before being consolidated into a pellet (5 mm diameter, ~3 mm height) via uniaxial pressure of 50 MPa. The pellet was placed on a molybdenum stage in the vacuum chamber of a Microwave Plasma Chemical Vapor Deposition (MPCVD) system (Wavemat Inc., Plymouth, MI, USA). The chamber was pumped to a base pressure of 1.1 Pa before adding a feedgas mixture (500 sccm Ar, 50 sccm H_2) and subsequent plasma ignition with a 2.45 GHz magnetron. H_2 in the feedgas was found to be necessary to concentrate and stabilize the plasma onto the sample. One of the benefits of using a MW-based BCTR process is that the dielectric metal oxides are expected to act as efficient microwave absorbers to allow the pellet to heat up rapidly (70–100 °C/min in our system) during the annealing process.[6]

The specimens were characterized by x-ray diffraction (XRD), nanoindentation, Vickers indentation, thermogravimetric analysis (TGA), micro-Raman spectroscopy, and scanning electron microscopy (SEM). A Panalytical Empyrean x-ray diffractometer (UK) with Cu-Kα radiation (λ = 1.54186 Å) was used at 45 kV and 40 mA, with 16.32 s/step and 0.0131° step size. An FEI Quanta FEG 650 (OR, USA) SEM was used for collecting images at an accelerating voltage of 15 kV. A Dilor XY confocal spectrometer (France) was used to conduct micro-Raman Spectroscopy (spot size ~1 μm) with a laser wavelength of 532 nm. Vickers hardness measurements were performed using a Phase II+ 900-390A Micro Vickers Hardness tester (TEquipment, Long Branch, NJ, USA). A test block of 711 HV (~7 GPa) was used before and after HEB samples to confirm calibration. Vickers indents were made using a dwell time of 15 s for loads up to a maximum of 200 gf. An Agilent Nano Indenter G200 (MTS Nano Instruments, Oak Ridge, TN, USA) was used to measure nanoindentation hardness in continuous stiffness mode with fused

TABLE I. Summary of material parameters from this work and other references for the same composition as HEB01.

	Composition	Excess B_4C (wt %)	Measured lattice constants c (Å)	a (Å)	Unit cell volume (Å)^3	Theoretical density[a] (g/cm^3) (relative density)	Vickers hardness (@ 200 gf) (GPa)
HEB01 (this work)	(Hf, Zr, Ti, Ta, Mo)B_2	9	3.090	3.359	27.78	8.40 (93.7%)	38 ± 3.6
HEB02 (this work)	(Hf, Zr, Nb, Ta, Mo)B_2	11	3.093	3.362	27.87	8.91 (92.1%)	34 ± 2.0
Reference 4	(Hf, Zr, Ti, Ta, Mo)B_2	···	3.080	3.316	27.24	8.4 (92.4%)	19.1 ± 1.8
Reference 16	(Hf, Zr, Ti, Ta, Mo)B_2	···	3.092	3.361	27.83	8.39 (98%)	30 ± 3.4
Reference 17	(Hf, Zr, Ti, Ta, Mo)B_2	14	3.092	3.366	27.87	8.37(99.9%)	24.9 ± 1.0

[a]The theoretical density was calculated using XRD lattice parameters.

silica as a calibration standard. Measurements confirmed that the silica modulus remained unchanged within 2% of its known value of 72 GPa after testing our samples. Nanoindentation was performed to a depth of 700 nm. Prior to Vickers and nanoindentation testing, the samples were mounted in epoxy, abraded with SiC papers (180–1500 grit), polished using diamond slurry (9–1 μm), and ultrasonically cleaned in isopropyl alcohol.

Thermal stability and decomposition behavior were studied via thermogravimetric analysis (TGA) using a TA Instruments model Q500 (DE, USA). The equipment was purged with compressed air at 100 and 10 ml/min for the furnace and sample, respectively. Samples were scanned from 30 to 1000 °C at a ramp rate of 2 °C/min, while data for sample weight loss were recorded as a function of temperature.

Density Functional Theory (DFT) calculations were performed to determine the Entropy Forming Ability (EFA)[14] for $(Hf_{0.2}Zr_{0.2}Ti_{0.2}Ta_{0.2}Mo_{0.2})B_2$ and $(Hf_{0.2}Zr_{0.2}Nb_{0.2}Ta_{0.2}Mo_{0.2})B_2$. To reproduce the stoichiometry, the minimum unit cell in the DFT calculations contains 15 atoms (e.g., $HfZrTiTaMoB_{10}$). The algorithm starts with the hexagonal AlB_2 structure (point group symmetry P6/mmm, space group No. 191) as the parent lattice. Each anion site is occupied by a B atom (with a probability of 1.0), whereas the cation site is occupied by five different transition-metal elements (with a 0.2 occupancy probability for each element). There are in total 84 distinct 15-atom-cell configurations (each having a degeneracy number g_i = 10),[14] which, in turn, are generated by the Automatic FLOW (AFLOW) partial occupation (AFLOW-POCC) method using Hermite normal form matrices.[18] Figure 1(a) displays some of the possible unit-cell structures.

The DFT calculations are based on the pseudopotential projected-augmented wave (PAW) method[19,20] using the Vienna *Ab Initio* Simulation Package (VASP).[21,22] The structure relaxation and electronic self-consistent calculations were conducted using the Perdew–Burke–Ernzerhof generalized gradient approximation (PBE-GGA) exchange-correlation functional.[23] We utilized a momentum space sampling of at least 6000 k-points per reciprocal atom (KPPRA) and a plane-wave cut-off energy of 446 eV (at least 1.4 times larger than the suggested cut-off energies in the VASP pseudopotentials). The convergence criteria of self-consistent and structural relaxation were set to 10^{-5} and 10^{-2} eV/Å, respectively.

For each POCC structure after the structure relaxation, VASP was also used to compute the elastic constants C_{ij} using the strain–stress method.[24] The elastic constants of each structure can help determine its corresponding mechanical properties, such as the bulk (K) and shear (G) moduli, using the Hill approximations by averaging over the Voigt and Reuss bounds.[25–27] With K and G, the Vickers hardness (H) of each structure can be estimated by the empirical hardness formula based on Chen's or Tian's models.[28,29] To compare with the hardness experiments, a statistical average over the hardness values of the POCC structures is performed. It is noted that the crystal symmetry of the original parent lattice can be slightly reduced due to the presence of different transition metal atoms. In this case, one should not assume that elastic constants C_{ij} retain the full symmetry properties of a hexagonal crystal.

III. RESULTS AND DISCUSSION

A. Calculations of entropy forming ability

In the EFA formalism,[14] the entropy content of a compound is estimated from the energy (or enthalpy) distribution spectrum h_i of each metastable configuration randomly sampled above the ground state. EFA is related to the inverse of the standard deviation σ associated with the spectral distribution: EFA = σ^{-1}, where $\sigma = \sqrt{\sum_i g_i (h_i - h_{mix})^2 / (\sum_i g_i - 1)}$. Here, the sum is over all distinct configurations, g_i is the degeneracy number of the ith configuration, and h_{mix} is the mixed-phase enthalpy approximated by averaging over h_i: $h_{mix} = \sum_i g_i h_i / \sum_i g_i$. Based on the above definition, the narrower the spectrum (σ), the higher the EFA value, and the higher the probability of forming high entropy single phases.

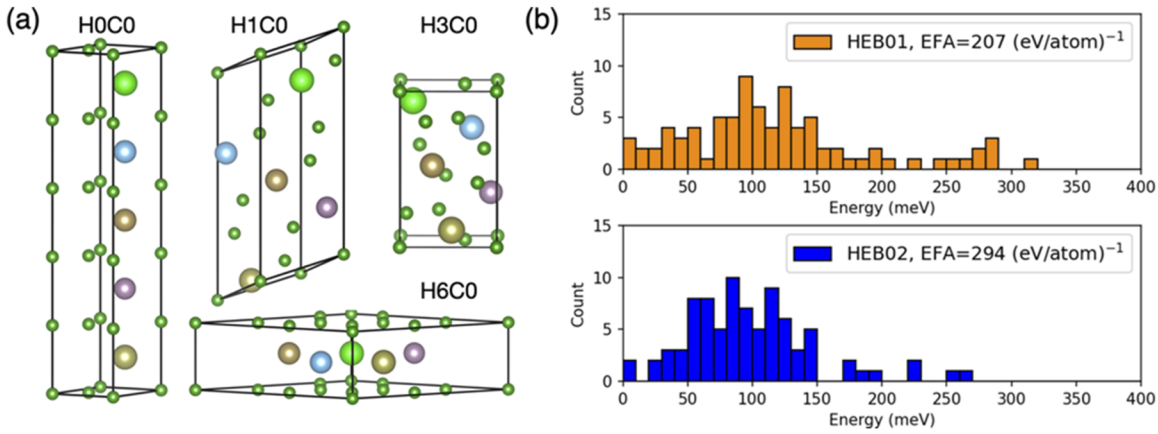

FIG. 1. (a) Selected crystal structures for a 15-atom unit-cell (5 different transition metal atoms and 10 boron atoms) generated from the AFLOW-POCC algorithm. (b) EFA calculation for $(Hf_{0.2}Zr_{0.2}Ti_{0.2}Ta_{0.2}Mo_{0.2})B_2$ (HEB01) is 207(eV/atom)$^{-1}$ and that for $(Hf_{0.2}Zr_{0.2}Nb_{0.2}Ta_{0.2}Mo_{0.2})B_2$ (HEB02) is 294(eV/atom)$^{-1}$. Higher-EFA means that the material is more easily synthesized in a single-phase form, which agrees with the experiments.

Figure 1(b) shows our EFA calculations for the two different HEBs under study. In $(Hf_{0.2}Zr_{0.2}Ti_{0.2}Ta_{0.2}Mo_{0.2})B_2$ (HEB01), the compound shows a wider energy distribution for the 84 distinct structures and a smaller EFA value of 207 $(eV/atom)^{-1}$. In contrast, $(Hf_{0.2}Zr_{0.2}Nb_{0.2}Ta_{0.2}Mo_{0.2})B_2$ (HEB02) has a relatively narrower energy distribution and a higher EFA value of 294 $(eV/atom)^{-1}$. As discussed below, these EFA results agree with our experimental findings that HEB02 (with a higher EFA) forms a single boride phase more easily. Together with previous studies on high entropy carbides,[14] our results demonstrate that the EFA can be a promising descriptor to predict the synthesizability of single phase high entropy materials. It should be noted that in a previous machine learning study on cubic high entropy carbides, EFA is found to be negatively correlated with the average ionic character and positively correlated with the liquidus temperature of the compound.[30] However, EFA, in general, can depend on several other features, such as the covalent radius and valence electrons.[30] Therefore, from a machine learning perspective, EFA is difficult to be predicted by a single feature, highlighting the need for a multivariate approach. Moreover, it is unknown if the aforementioned trends reported for cubic high entropy carbides apply to hexagonal high entropy borides. Addressing this question would require the knowledge of EFA values for at least a few tens of hexagonal High Entropy (HE) borides for target-feature analysis, which is an interesting area of future study but beyond the scope of the current work.

B. Phase composition

Both HEB formulations (HEB01 and HEB02) were synthesized for MW plasma annealing temperatures of 1500 and 2000 °C, respectively, and then examined by XRD to determine how the two different processing temperatures affect structural evolution, leading to the desired single hexagonal high entropy phase.

XRD patterns of the annealed samples are shown in Fig. 2 for both MW plasma processing temperatures. For reference, line indicators are also shown where individual diborides, as well as B_4C and graphite, would occur, if present. The hexagonal phase marked by the Miller indices identifies the expected presence of the high entropy boride structure. Lattice constants and unit cell volume for the hexagonal phase structure were determined using Rietveld refinement and tabulated in Table I. When comparing the HEBs annealed at 1500 °C, the XRD peaks from the high entropy phase for HEB02 are more intense with less indication of secondary phases (i.e., B_4C and individual diborides) than that for HEB01. However, both formulations still show secondary phase formation at this temperature. For both HEB01 and HEB02, annealing at 2000 °C presents very high crystalline phase purity that can be indexed to the single hexagonal structure expected for high entropy boride. Although very weak, residual B_4C peaks can be found in the 2θ range of 35°–40° even at this temperature. These XRD results are consistent with the higher EFA calculated for HEB02 compared to HEB01 and demonstrate that the HEB02 formulation (Hf, Zr, Nb, Ta, Mo)B_2 allows more rapid completion to the high entropy phase at a lower temperature than for HEB01 (Hf, Zr, Ti, Ta, Mo)B_2. The unit cell volumes for HEB01 and HEB02 determined from Rietveld analysis are in close agreement with those found for the same configuration as determined by other groups experimentally[4,16,17] and computationally.[31]

C. Thermogravimetric analysis

One of the outstanding predicted properties of HEBs is their thermal stability at high temperatures. To this end, thermogravimetric analysis was used to evaluate weight gain vs temperature in controlled airflow. In addition to the plasma annealed samples (HEB01 and HEB02 synthesized at 2000 °C), control samples were tested including an individual commercial diboride powder (TiB_2) as well as an equal-molar mixture consisting of the five commercial diboride powders (HfB_2, ZrB_2, TiB_2, TaB_2, MoB_2). The goal of these measurements is to confirm the improved oxidation resistance performance of our samples compared to "off-the-shelf" formulations as further validation of their high-entropy nature. The TGA data in Fig. 3 reveal the plasma annealed HEB samples with much lower weight gain (as much as a factor of ten reductions for HEB01)

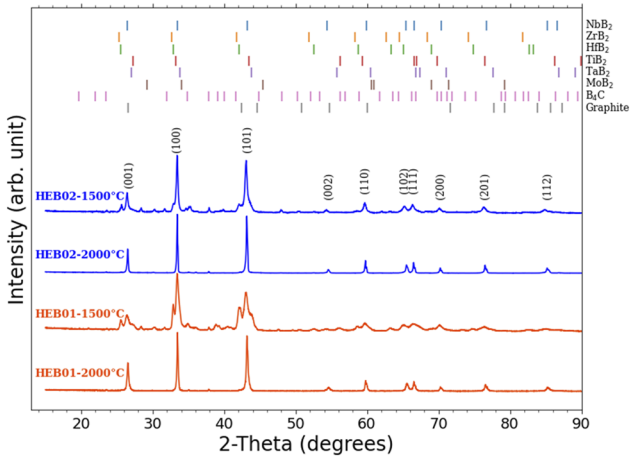

FIG. 2. XRD patterns of HEB samples annealed at different temperatures (1500 and 2000 °C) for HEB01 (orange) and HEB02 (blue). All samples were MW plasma annealed for 45 min.

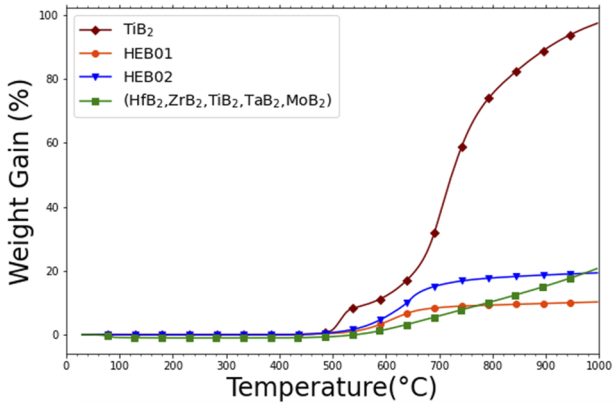

FIG. 3. Weight gain (in the air) vs sample temperature measured from the thermogravimetric analysis. Samples measured include the plasma annealed HEBs made at 2000 °C: HEB01 (orange), HEB02 (blue), a mixture consisting of five commercial diborides (green), and TiB_2 (brown).

when compared to the TiB_2 sample at 1000 °C. In addition, the rate of weight gain with temperature tapers off above 650 °C for both HEB01 and HEB02 samples, approaching a saturation weight gain of 10.2% and 19.3%, respectively. By comparison, the control sample consisting of a mixture of five commercial diborides (HfB_2, ZrB_2, TiB_2, TaB_2, MoB_2) shows a steady increase in weight gain starting at 600 °C. Although promising, these data are not proof that the plasma process itself is providing enhanced oxidation resistance above and beyond the high-entropy nature of the samples. Reports of oxidation resistance for HEBs are scarce, but the reports typically show accelerated weight gain above 1100–1200 °C.[4,32] The HEB samples in this study will need to be tested at higher temperatures in order to more critically evaluate the potential benefit of MW plasma processing on oxidation resistance.

Interestingly, the HEB01 sample exhibited reduced weight gain by a factor of about two compared to HEB02. The only difference between these two samples is the presence of Ti in HEB01 substituting for Nb in HEB02, leading to a lower calculated EFA for HEB01. The EFA descriptor captures the relative propensity of a material to form a high-entropy single-phase crystal structure.

D. Vickers and nanoindentation hardness

The Vickers hardness at a given load was measured, on average, to be higher for HEB01 than for HEB02, as shown in Fig. 4. The hardness was measured for loads of 10–200 gf in order to identify a possible indentation size effect (ISE). Each indent load represented in Fig. 4 is the average of ten indents placed on the polished surface of the sample. At a maximum load of 200 gf, measured hardness values for HEB01 and HEB02 were 38 ± 3.6 and 34 ± 2.0 GPa, respectively. Vickers hardness measurements performed using the same load and dwell time for HEBs having the same chemical configuration as HEB01 (in this study) have been reported by Gild *et al.* as 24.9 ± 1.0 GPa[17] and by Feng *et al.*[16] as 30.6 ± 3.4 GPa; both reports used BCTRT followed by spark plasma sintering. At 1000 gf (9.8 N), Feng reported a drop in this hardness to 25.0 ± 0.5 GPa.

Indeed, hardness is not considered a fundamental material property and is often prone to the so-called Indentation Size Effect (ISE).[33] The ISE is characterized by increasing hardness with decreasing indent load, as is often found in many structural ceramics and other material types.[3,16] The ISE effect can be evaluated most simply using Meyer's power law[34] by plotting load vs indent diagonal, as shown in Fig. 5 for HEB01 and HEB02. This law is used to understand the ISE behavior of the material based on the formula $F = Ad^n$, where F is the applied load, A is the standard microhardness constant, d is the indent diagonal length, and n represents the Meyer index. Both HEB samples reveal normal ISE behavior corresponding to $n < 2$. The hardness values listed in Table I are for indents made at 200 gf, and it is possible that these values would be measured lower with higher indent loads according to the ISE. Nevertheless, the higher average hardness at an indent load of 200 gf found from HEB samples in this study is promising and will require further study into the influence of microstructure (e.g., grain size) on this measurement. In our previous study of HEBs made using the MW plasma approach,[5] transmission electron microscopy revealed individual grains with an estimated average size of 20 nm. while SEM revealed an average particle size of 165 nm.

To complement and validate the Vickers hardness measurement, nanoindentation measurements were performed for both HEB01 and HEB02 polished disks to an indent depth of 700 nm. Figure 6(a) shows a characteristic SEM image of the high entropy boride after polishing. For each of HEB01 and HEB02, 15–20 indents were made to provide an average with standard deviation, as given in Table II. The corresponding hardness vs displacement data are shown in Fig. 6(b) for each HEB sample along with a fused silica standard. The variation in hardness with depth for the HEB samples may be due to the larger influence of surface roughness on nanoindentation and/or the effect of small local variations in composition at the scale of the nanoindenter probe volume. Nevertheless, the average values presented in Table I are consistent with the Vickers data, indicating that HEB01 (36.1 ± 3.0 GPa) has a higher hardness than HEB02 (32.0 ± 6.5 GPa).

The hardness values measured in this study (both by Vickers and nanoindentation) are significantly higher than what has been reported for similar HEB configurations, as presented in Table I. The measured relative density of our HEB samples (~92%–94%) is also

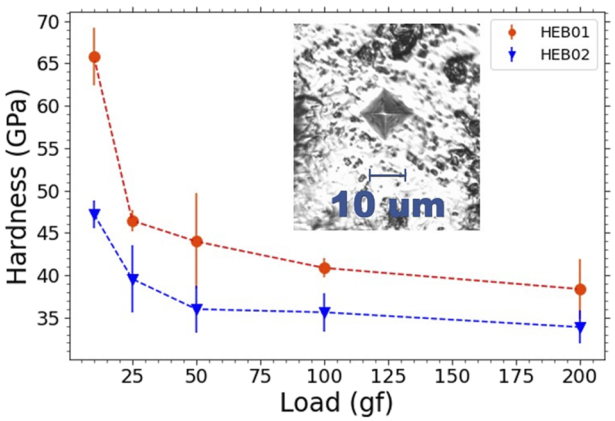

FIG. 4. Vickers hardness vs indent load for the HEB samples made at 2000 °C. Inset shows an optical micrograph of an indent made on the HEB02 sample surface at 200 gf.

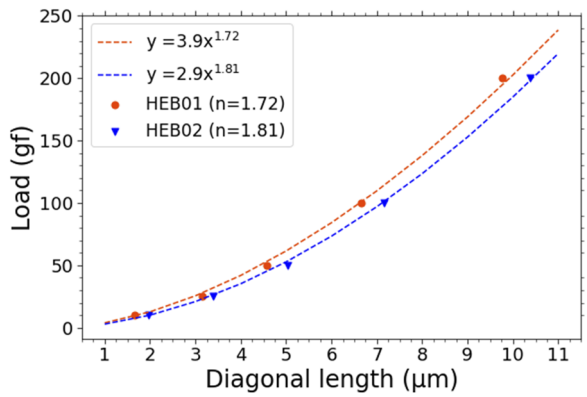

FIG. 5. The applied Vickers load vs indent diagonal length for both HEB samples made in this study at 2000 °C. The Meyer index of $n < 2$ for each sample indicates a normal indentation size effect (ISE).

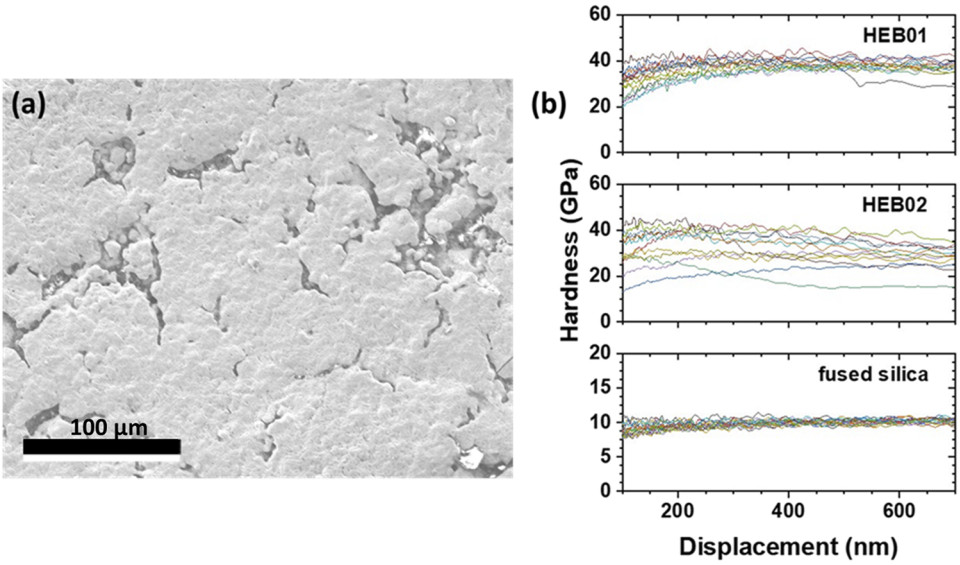

FIG. 6. (a) Representative SEM image from the polished high entropy boride HEB02 sample synthesized in this study at 2000 °C. (b) Hardness vs displacement for HEB01, HEB02, and fused silica standard (nominal hardness = 9.5 GPa).

lower than that typically obtained for spark plasma-sintered HEB samples, which can be nearly 100%. Nevertheless, some degree of microwave-induced sintering occurs with our HEB samples, leading to localized regions of high density, despite the measured overall lower relative density. We deliberately chose indent locations away from obvious surface pores, and we anticipate that the effective local density probed by the indenter is higher than that reported on the scale of Vickers indentation depths. It is promising that nanoindentation validates the Vickers indentation results since nanoindentation depths are expected to be even less sensitive to macroscopic pores (which were also deliberately avoided during indentation).

E. Hardness computations

The POCC method for computing EFA can also be utilized to compute the mechanical properties of high entropy materials. Figure 7(a) shows the hardness distribution of the 84 distinct POCC structures for a 15-atom hexagonal boride unit cell. To compare with experiments, we compute an average hardness from the POCC results using the Boltzmann distribution, as a function of the "synthesis" temperature. As shown in Fig. 7(b), the theoretical results indicate that the hardness would decrease with increasing synthesis temperature, as the low-enthalpy POCC structure exhibits a higher hardness in our calculations for both HEBs. However, the hardness variation for synthesis temperature at >1000 K is smaller than our experimental uncertainty. The hardness values of ~33 and 31.5 GPa at high synthesis temperature, respectively, for HEB01 and HEB02, agree with the measurements within experimental error bars. The theoretical hardness of HEB01 is larger than HEB02, again consistent with experiments.

In this study, we find that replacing Nb with Ti in the HEB configuration results in higher measured hardness. This trend is also validated by the hardness computations (for a given processing temperature). These data can be explained by the lattice distortion effect caused by the different atomic sizes and elastic modulus mismatch of Ti vs Nb in the HEB configurations. Given that the atomic radius of Ti is smaller than that of Nb, the resulting lattice distortion can affect hardness by limiting the motion of dislocations necessary for plastic deformation, as well as changes in the slip systems and the ease with which slip can occur. This well-known effect also manifests itself in high entropy ceramics;[35] for example, superhard high-entropy transition metal monoborides were reported with a Vickers hardness of 48.51 ± 4.07 GPa measured at 0.49 N.[36] These borides revealed a high density of dislocations pinned within the monoboride grains, indicating severe lattice distortion. One important reason for the severe lattice distortion is that the individual components have not only atomic radius mismatches but also different types of crystal structures.

TABLE II. Average nanoindentation hardness and Young's modulus for the HEB samples in this study.

	Average nanoindentation hardnessb (No. of indents per sample: 15–20, depth: 100–700 nm)	
Sample	Hardness (GPa)	Young's modulus (GPa)
HEB01	36.1 ± 3.0	417 ± 34
HEB02	32.0 ± 6.5	386 ± 79
Fused silica	9.2 ± 0.3	72.2 ± 1.4

F. Residual impurity

In our prior work,[5] we demonstrated excellent compositional uniformity of metal cations throughout the HEB structure using energy dispersive X-ray microanalysis (EDX). Here, we note that micro-Raman spectroscopy is a particularly suitable technique for probing the presence of residual carbon in its various allotropic forms and also reveals boron carbide[37] as well as some metal oxides if present. Given the potential for compositional inhomogeneity due to excess carbon, oxides, and/or boron carbide powder precursors

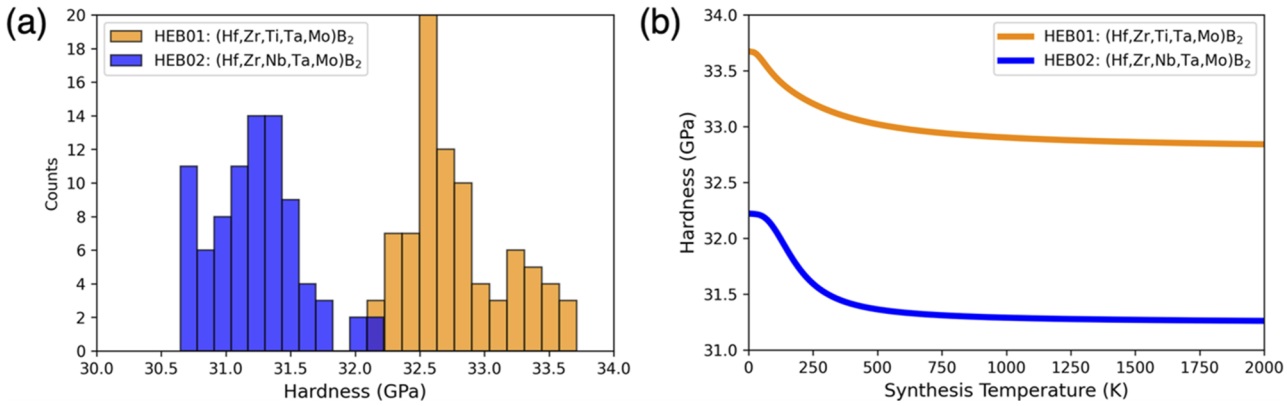

FIG. 7. (a) Histograms of hardness distribution computed for the 84 distinct HEB POCC structures. (b) Averaged hardness using the Boltzmann distribution as a function of the "synthesis" temperature. HEB01 is found to be harder than HEB02, consistent with the experiments.

used for BCTR processing, the HEB MW-plasma annealed pellets were crushed into a fine powder and placed on a glass slide for Raman measurements. Figure 8 shows micro-Raman spectra (spot size ~1 μm) for both HEB01 and HEB02 synthesized at 2000 °C after probing several locations that yielded only background noise with no distinctive Raman signature. Despite XRD showing a predominantly single-phase hexagonal structure for the HEB samples annealed at 2000 °C, micro-Raman spectroscopy showed minor evidence of the G-band associated with residual graphite (peak c.a. 1580 cm^{-1}) at some locations tested within the HEB02 powder. Raman spectra in the range 200–800 cm^{-1} (where several metal-oxides manifest themselves) were also unremarkable and, therefore, not shown here. Nevertheless, other studies of sintered HEBs have reported oxygen impurities in different forms including a thin (~3–5 nm) amorphous B_2O_3 layer surrounding individual boride grains.[38] Residual unreacted metal oxides have also been observed in sintered HEBs.[39] It is possible that these could form very fine oxide dispersions, as with high entropy alloys.[40] Of the transition metals used here, the most likely residual metal-oxide candidate would be

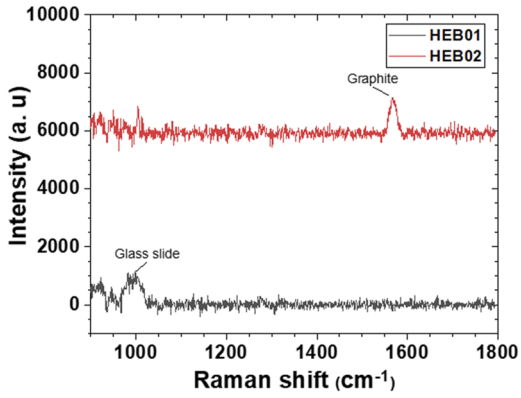

FIG. 8. Selected Raman spectra (background subtracted) of the HEBs in powder form for (a) HEB01 and (b) HEB02, both samples synthesized at 2000 °C.

HfO_2 due to its relative thermodynamic stability at the processing temperatures used. In any case, any residual oxides presented in our HEB samples plasma processed at 2000 °C could not be detected, at least by XRD or Raman spectroscopy. Since nanoindentation measurements on both HEB01 and HEB02 pellet surfaces reveal a wide distribution of hardness (as low as 15 GPa to as high as 45 GPa) depending on test location, these results suggest compositional inhomogeneity, at least at the scale of nanoindentation and micro-Raman probe volumes.

IV. CONCLUSION

A single 45-min annealing step using microwave-induced plasma to create HEBs validates the higher entropy-forming ability for HEB02: (Hf, Zr, Nb, Ta, Mo)B_2 compared to HEB01: (Hf, Zr, Ti, Ta, Mo)B_2 based on x-ray diffraction of these materials annealed at either 1500 or 2000 °C. While both HEB configurations annealed at 2000 °C reveal a predominantly single-phase hexagonal crystal structure, conversion to the high-entropy phase was more complete for HEB02 at 1500 °C. These XRD results are consistent with calculations of EFA for the two configurations giving a higher EFA for HEB02: 294 $(eV/atom)^{-1}$ than that of HEB01: 207 $(eV/atom)^{-1}$. Nevertheless, hardness measurements (both Vickers and nanoindentation), as well as TGA oxidation resistance measurements, show better performance on average for HEB01. Both HEB configurations evaluated in this study yield hardness values as much as 50% higher than that reported in other studies for the same chemical configuration and testing load. However, the large spread in hardness values in this study (depending on indent location) as well as the minor presence of graphite found at some locations within HEB02 indicate phase inhomogeneity at the micrometer scale. Oxidation resistance for the plasma annealed HEBs (measured as weight gain) is improved by as much as a factor of ten when compared to conventional commercial diborides and shows a plateau above 650 °C. Overall, these results point to the exceptional potential for the microwave-induced plasma annealing method. Future studies are needed to identify grain boundary composition/structure as well as

to improve the homogeneity of the high-entropy phase (and material properties) throughout the bulk of the sample.

ACKNOWLEDGMENTS

This work was supported by National Science Foundation (NSF) EPSCoR RII Track-1 Cooperative Agreement No. OIA-1655280. Any opinions, findings, and conclusions or recommendations expressed in this material are those of the authors and do not necessarily reflect the views of the National Science Foundation. The authors thank Paul A. Baker for assistance with SEM measurements.

AUTHOR DECLARATIONS

Conflict of Interest

The authors have no conflicts to disclose.

Author Contributions

Bria Storr: Formal analysis (lead); Investigation (lead); Writing – original draft (equal). **Luke Moore:** Formal analysis (equal); Investigation (equal). **Kallol Chakrabarty:** Formal analysis (supporting); Investigation (supporting). **Zaheeruddin Mohammed:** Formal analysis (supporting); Investigation (supporting); Methodology (supporting). **Vijaya Rangari:** Investigation (supporting); Supervision (supporting). **Cheng-Chien Chen:** Formal analysis (equal); Investigation (equal); Supervision (equal); Writing – review & editing (equal). **Shane A. Catledge:** Conceptualization (equal); Investigation (equal); Methodology (equal); Project administration (equal); Supervision (equal); Writing – review & editing (equal).

DATA AVAILABILITY

The data that support the findings of this study are available from the corresponding authors upon reasonable request.

REFERENCES

[1]A. Nisar, C. Zhang, B. Boesl, and A. Agarwal, "A perspective on challenges and opportunities in developing high entropy-ultra high temperature ceramics," Ceram. Int. **46**(16), 25845–25853 (2020).
[2]L. Feng, W. G. Fahrenholtz, and G. E. Hilmas, "Two-step synthesis process for high-entropy diboride powders," J. Am. Ceram. Soc. **103**(2), 724–730 (2020).
[3]J. Gu, J. Zou, S.-K. Sun, H. Wang, S.-Y. Yu, J. Zhang, W. Wang, and Z. Fu, "Dense and pure high-entropy metal diboride ceramics sintered from self-synthesized powders *via* boro/carbothermal reduction approach," Sci. China Mater. **62**(12), 1898–1909 (2019).
[4]J. Gild, Y. Zhang, T. Harrington, S. Jiang, T. Hu, M. C. Quinn, W. M. Mellor, N. Zhou, K. Vecchio, and J. Luo, "High-entropy metal diborides: A new class of high-entropy materials and a new type of ultrahigh temperature ceramics," Sci. Rep. **6**(1), 37946 (2016).
[5]B. Storr, D. Kodali, K. Chakrabarty, P. A. Baker, V. Rangari, and S. A. Catledge, "Single-step synthesis process for high-entropy transition metal boride powders using microwave plasma," Ceramics **4**(2), 257–264 (2021).
[6]J. Sun, W. Wang, and Q. Yue, "Review on microwave-matter interaction fundamentals and efficient microwave-associated heating strategies," Materials **9**(4), 231 (2016).
[7]I. Adamovich, S. D. Baalrud, A. Bogaerts, P. J. Bruggeman, M. Cappelli, V. Colombo, U. Czarnetzki, U. Ebert, J. G. Eden, P. Favia, D. B. Graves, S. Hamaguchi, G. Hieftje, M. Hori, I. D. Kaganovich, U. Kortshagen, M. J. Kushner, N. J. Mason, S. Mazouffre, S. M. Thagard, H.-R. Metelmann, A. Mizuno, E. Moreau, A. B. Murphy, B. A. Niemira, G. S. Oehrlein, Z. L. Petrovic, L. C. Pitchford, Y.-K. Pu, S. Rauf, O. Sakai, S. Samukawa, S. Starikovskaia, J. Tennyson, K. Terashima, M. M. Turner, M. C. M. van de Sanden, and A. Vardelle, "The 2017 Plasma Roadmap: Low temperature plasma science and technology," J. Phys. D: Appl. Phys. **50**(32), 323001 (2017).
[8]A. Fridman, *Plasma Chemistry* (Cambridge University Press, New York, 2008).
[9]D. van den Bekerom, N. den Harder, T. Minea, N. Gatti, J. P. Linares, W. Bongers, R. van de Sanden, and G. van Rooij, "Non-equilibrium microwave plasma for efficient high temperature chemistry," J. Visualized Exp. **2017**(126), e55066.
[10]R. R. Menezes, P. M. Souto, and R. H. G. A. Kiminami, "Microwave hybrid fast sintering of porcelain bodies," J. Mater. Process. Technol. **190**(1), 223–229 (2007).
[11]P. Yadoji, R. Peelamedu, D. Agrawal, and R. Roy, "Microwave sintering of Ni–Zn ferrites: Comparison with conventional sintering," Mater. Sci. Eng., B **98**(3), 269–278 (2003).
[12]C. Leonelli, P. Veronesi, L. Denti, A. Gatto, and L. Iuliano, "Microwave assisted sintering of green metal parts," J. Mater. Process. Technol. **205**(1), 489–496 (2008).
[13]D. E. Clark, D. C. Folz, and J. K. West, "Processing materials with microwave energy," Mater. Sci. Eng., A **287**(2), 153–158 (2000).
[14]P. Sarker, T. Harrington, C. Toher, C. Oses, M. Samiee, J. P. Maria, D. W. Brenner, K. S. Vecchio, and S. Curtarolo, "High-entropy high-hardness metal carbides discovered by entropy descriptors," Nat. Commun. **9**(1), 4980 (2018).
[15]T. J. Harrington, J. Gild, P. Sarker, C. Toher, C. M. Rost, O. F. Dippo, C. McElfresh, K. Kaufmann, E. Marin, L. Borowski, P. E. Hopkins, J. Luo, S. Curtarolo, D. W. Brenner, and K. S. Vecchio, "Phase stability and mechanical properties of novel high entropy transition metal carbides," Acta Mater. **166**, 271–280 (2019).
[16]L. Feng, F. Monteverde, W. G. Fahrenholtz, and G. E. Hilmas, "Superhard high-entropy AlB_2-type diboride ceramics," Scr. Mater. **199**, 113855 (2021).
[17]J. Gild, A. Wright, K. Quiambao-Tomko, M. Qin, J. A. Tomko, M. Shafkat bin Hoque, J. L. Braun, B. Bloomfield, D. Martinez, T. Harrington, K. Vecchio, P. E. Hopkins, and J. Luo, "Thermal conductivity and hardness of three single-phase high-entropy metal diborides fabricated by borocarbothermal reduction and spark plasma sintering," Ceram. Int. **46**(5), 6906–6913 (2020).
[18]K. Yang, C. Oses, and S. Curtarolo, "Modeling off-stoichiometry materials with a high-throughput ab-initio approach," Chem. Mater. **28**(18), 6484–6492 (2016).
[19]G. Kresse and D. Joubert, "From ultrasoft pseudopotentials to the projector augmented-wave method," Phys. Rev. B **59**, 1758–1775 (1999).
[20]P. E. Blöchl, "Projector augmented-wave method," Phys. Rev. B **50**(24), 17953–17979 (1994).
[21]G. Kresse and J. Furthmüller, "Efficiency of ab-initio total energy calculations for metals and semiconductors using a plane-wave basis set," Comput. Mater. Sci. **6**(1), 15–50 (1996).
[22]G. Kresse and J. Furthmüller, "Efficient iterative schemes for *ab initio* total-energy calculations using a plane-wave basis set," Phys. Rev. B **54**(16), 11169–11186 (1996).
[23]J. P. Perdew, K. Burke, and M. Ernzerhof, "Generalized gradient approximation made simple," Phys. Rev. Lett. **77**, 3865–3868 (1996).
[24]Y. Le Page and P. Saxe, "Symmetry-general least-squares extraction of elastic data for strained materials from *ab initio* calculations of stress," Phys. Rev. B **65**(10), 104104 (2002).
[25]R. Hill, "The elastic behaviour of a crystalline aggregate," Proc. Phys. Soc., Sect. A **65**(5), 349–354 (1952).
[26]W. Voigt, *Lehrbuch der Kristallphysik (mit Ausschluss der Kristalloptik)* (BG Teubner, 1910), Vol. 34.
[27]A. Reuss, "Berechnung der Fließgrenze von Mischkristallen auf Grund der Plastizitätsbedingung für Einkristalle," Z. Angew. Math. Mech. **9**(1), 49–58 (1929).
[28]X.-Q. Chen, H. Niu, D. Li, and Y. Li, "Modeling hardness of polycrystalline materials and bulk metallic glasses," Intermetallics **19**(9), 1275–1281 (2011).
[29]Y. Tian, B. Xu, and Z. Zhao, "Microscopic theory of hardness and design of novel superhard crystals," Int. J. Refract. Met. Hard Mater. **33**, 93–106 (2012).

[30]K. Kaufmann, D. Maryanovsky, W. M. Mellor, C. Zhu, A. S. Rosengarten, T. J. Harrington, C. Oses, C. Toher, S. Curtarolo, and K. S. Vecchio, "Discovery of high-entropy ceramics via machine learning," npj Comput. Mater. **6**(1), 1–9 (2020).
[31]J.-X. Liu, X.-Q. Shen, Y. Wu, F. Li, Y. Liang, and G.-J. Zhang, "Mechanical properties of hot-pressed high-entropy diboride-based ceramics," J. Adv. Ceram. **9**(4), 503–510 (2020).
[32]G. Tallarita, R. Licheri, S. Garroni, S. Barbarossa, R. Orrú, and G. Cao, "High-entropy transition metal diborides by reactive and non-reactive spark plasma sintering: A comparative investigation," J. Eur. Ceram. Soc. **40**(4), 942–952 (2020).
[33]Y. V. Milman, A. A. Golubenko, and S. N. Dub, "Indentation size effect in nanohardness," Acta Mater. **59**(20), 7480–7487 (2011).
[34]J. Gong, J. Wu, and Z. Guan, "Analysis of the indentation size effect on the apparent hardness for ceramics," Mater. Lett. **38**(3), 197–201 (1999).
[35]H. Xiang, Y. Xing, F.-z. Dai, H. Wang, L. Su, L. Miao, G. Zhang, Y. Wang, X. Qi, L. Yao, H. Wang, B. Zhao, J. Li, and Y. Zhou, "High-entropy ceramics: Present status, challenges, and a look forward," J. Adv. Ceram. **10**(3), 385–441 (2021).
[36]P. Zhao, J. Zhu, Y. Zhang, G. Shao, H. Wang, M. Li, W. Liu, B. Fan, H. Xu, H. Lu, Y. Zhou, and R. Zhang, "A novel high-entropy monoboride $(Mo_{0.2}Ta_{0.2}Ni_{0.2}Cr_{0.2}W_{0.2})B$ with superhardness and low thermal conductivity," Ceram. Int. **46**(17), 26626–26631 (2020).
[37]E. I. Bîru and H. Iovu, "Graphene nanocomposites studied by Raman spectroscopy," Raman Spectrosc. **9**, 179 (2018).
[38]B. Ye, C. Fan, Y. Han, M. Ma, and Y. Chu, "Synthesis of high-entropy diboride nanopowders via molten salt-mediated magnesiothermic reduction," J. Am. Ceram. Soc. **103**(9), 4738–4741 (2020).
[39]Y. Zhang, Z.-B. Jiang, S.-K. Sun, W.-M. Guo, Q.-S. Chen, J.-X. Qiu, K. Plucknett, and H.-T. Lin, "Microstructure and mechanical properties of high-entropy borides derived from boro/carbothermal reduction," J. Eur. Ceram. Soc. **39**(13), 3920–3924 (2019).
[40]J. He, Y. Qiao, R. Wang, Y. Tang, S. Li, X. Liu, Y. Ye, L. Zhu, Z. Wang, and S. Bai, "State and effect of oxygen on high entropy alloys prepared by powder metallurgy," J. Alloys Compd. **891**, 161963 (2022).